

The calcite → aragonite transformation in low-Mg marble: Equilibrium relations, transformation mechanisms, and rates

Bradley R. Hacker,¹ David C. Rubie,² Stephen H. Kirby,³ and Steven R. Bohlen⁴

Received 6 July 2004; revised 19 December 2004; accepted 3 January 2005; published 19 March 2005.

[1] Experimental transformation of a rather pure natural calcite marble to aragonite marble did not proceed via the expected straightforward polymorphic replacement. Instead, the small amount of Mg in the starting material (0.36 wt %) was excluded from the growing aragonite and diffused preferentially into the remaining calcite grains, producing Mg-rich calcite rods that persisted as relicts. Nucleation of aragonite occurred exclusively on grain boundaries, with aragonite [001] oriented subparallel to calcite [0001]. The aragonite crystals preferentially consumed the calcite crystal on which they nucleated, and the reaction fronts developed preferentially along the {010} and {110} planes of aragonite. Each aragonite neoblast that grew was nearly free of Mg (typically <0.1 wt %). The excess Mg was taken up by the calcite grains in between, stabilizing them and causing a few volume percent rodlike relicts of Mg-enriched calcite (up to 10 wt % MgO) to be left behind by the advancing reaction front. The aragonite growth rates are approximately linear and range from $\sim 3 \times 10^{-11} \text{ m s}^{-1}$ at 600°C to $\sim 9 \times 10^{-9} \text{ m s}^{-1}$ at 850°C, with an apparent activation enthalpy of $166 \pm 91 \text{ kJ mol}^{-1}$. This reaction mechanism and the resultant texture are akin to cellular precipitation reactions in metals. Similar transformation textures have been reported from high-Mg marbles in Japan and China that disproportionated to low-Mg calcite and dolomite.

Citation: Hacker, B. R., D. C. Rubie, S. H. Kirby, and S. R. Bohlen (2005), The calcite → aragonite transformation in low-Mg marble: Equilibrium relations, transformation mechanisms, and rates, *J. Geophys. Res.*, 110, B03205, doi:10.1029/2004JB003302.

1. Introduction

[2] Understanding the mechanisms and rates at which solid-solid mineral reactions occur is important for understanding many aspects of Earth behavior, including, for example, phase transformations in subducting slabs [Rubie and Ross, 1994] and the gravitational (in)stability of the lower crust [Jull and Kelemen, 2001]. This study seeks to bridge this gap by comprehensively documenting the transformation mechanism of polycrystalline calcite to aragonite in solid marble. We chose to study the calcite → aragonite transformation because it is a nominally simple, yet geologically important, reaction often considered the mineralogical archetype of isochemical, reconstructive phase changes. The reverse reaction, aragonite → calcite, has been the focus of several important studies of mineralogical phase transformations [e.g., Carlson and Rosenfeld, 1981].

2. Experimental Method

2.1. Starting Material

[3] Most kinetic experiments on geologic materials have started with either single crystals or powdered grains, physical states quite different from rocks in much of the Earth. Results from such experiments are in general inapplicable to many natural situations for reasons enumerated by Rubie and Thompson [1985]. Our starting material is a single block of Carrara marble obtained from a monument company [Hacker and Kirby, 1993, Figure 3A]. The only impurities present above optical spectroscopy detection limits (generally 5 ppm) in a powder of the bulk rock are 0.36 wt % MgO, 0.2 wt % FeO, 130 wt ppm Sr, and 49 wt ppm MnO. These values are typical of marine carbonates [Veizer, 1978] and are equivalent to 0.16 mol % FeCO₃ and 0.50 mol % MgCO₃. No phases other than calcite were detected by X-ray powder diffraction or optical microscopy. Transmission electron microscopy (TEM) revealed very rare 1 μm diopside crystals. The grain size measured in thin section by the mean linear intercept method is 78 μm, and converting this to an actual mean grain diameter [Gifkins, 1970] gives a grain size of 117 μm. There is no shape-preferred orientation or lattice-preferred orientation detectable using optical microscopy. Most grains contain twins spaced $\sim 25 \mu\text{m}$ apart and possess weak undulatory extinction; a few grains have low-angle subgrain boundaries that are generally subperpendicular to the twins. Grain boundaries are curvilinear, indicating that the marble

¹Department of Geological Sciences, University of California, Santa Barbara, California, USA.

²Bayerisches Geoinstitut, Universität Bayreuth, Bayreuth, Germany.

³U.S. Geological Survey, Menlo Park, California, USA.

⁴Joint Oceanographic Institutions, Washington, D. C., USA.

Table 1. Calcite ↔ Aragonite Equilibrium Experiments^a

Experiment	T, K	P, GPa	t, hours:min	Result
<i>Interpretation: Reversal at 873 K and 1.49 ± 0.10 (±0.05) GPa</i>				
1-1147	873	1.47	87:20	C grew
1-1153	873	1.49	70:50	no change
1-1142	873	1.51	54:15	A grew
1-1138	873	1.53	39:25	A grew
<i>Interpretation: Reversal at 973 K and 1.87 ± 0.11 (±0.06) GPa</i>				
1-1140	973	1.77	61:30	all C
1-1155	973	1.82	38:55	all C
1-1208	973	1.84	89:05	C grew
1-1156	973	1.84	44:55	all C
1-1152	973	1.86	22:20	no change
1-1206	973	1.86	38:45	no change
1-1207	973	1.88	49:00	no change
1-1150	973	1.90	22:00	A grew
<i>Interpretation: Reversal at 1073 K and 2.31 ± 0.09 (±0.04) GPa</i>				
1-1139	1073	2.02	21:55	mostly C
1-1141	1073	2.10	15:50	all C
1-1144	1073	2.30	14:50	mostly C
1-1154B	1073	2.32	7:35	A grew
1-1148	1073	2.34	19:50	A grew
1-1145	1073	2.38	6:10	A grew
<i>Interpretation: Reversal at 873 K and 1.55 ± 0.09 (±0.04) GPa</i>				
2-1391	873	1.54	8:00	C grew
2-1390	873	1.56	6:00	A grew
<i>Interpretation: Reversal at 1073 K and 2.39 ± 0.09 (±0.04) GPa</i>				
2-1376	1073	2.26	24:05	all C
2-1378	1073	2.28	6:00	mostly C
2-1380	1073	2.30	6:00	all C
2-1383	1073	2.34	6:00	all C
2-1385	1073	2.38	7:15	all C
2-1387	1073	2.40	6:00	A grew
2-1386	1073	2.42	8:00	A grew

^aA, aragonite; C, calcite. First digit of experiment number indicates apparatus 1 or 2. First uncertainty given for pressure is for absolute pressure; the uncertainty in parentheses is for relative pressures among a group of experiments at the same *T* and *P* conducted within a single apparatus.

has not reached complete textural equilibrium. Transmission electron microscopy reveals a rather uniform distribution of dislocations with a density of 10^{12} – 10^{13} m⁻². About one-third are simple, straight unit dislocations, whereas the remainder are in curved segments, complex tangles, and individual dislocation loops.

2.2. Experimental Techniques

[4] Although the chief objectives of this work were to measure the rates and mechanisms of the calcite → aragonite transformation, we also performed reversal experiments

to locate the calcite-aragonite equilibrium boundary precisely in each of our two apparatuses (Table 1). Both types of experiment were conducted in piston-cylinder apparatus using NaCl as a confining medium in 1-inch inner-diameter pressure vessels [Bohlen, 1984]; the pressure on the sample was assumed to be 140 MPa greater than the gauge pressure, based on calibration experiments at 1.4–2.0 GPa by C. Manning and J. Hayob.

[5] Pressures in the piston cylinder apparatus can typically be maintained to within ± 20 MPa during an experiment, such that the relative uncertainty among different runs in the same press is $\sqrt{20^2 + 20^2}$ or ~30 MPa. Prior to our investigation, both of our apparatuses were calibrated with the albite = jadeite + quartz equilibrium. Both apparatuses showed reversal of that equilibrium within 50 MPa of the “correct” pressure [Johannes *et al.*, 1971] at 600°C; thus the uncertainty in the absolute pressures of our calcite-aragonite experiments is $\sim 50 \pm 20$ MPa. As discussed below, reversals of the calcite-aragonite equilibrium indicate a systematic pressure difference between our apparatus 1 and apparatus 2 of 60–80 MPa. Table 1 shows that a few experiments experienced (usually brief) excursions from the nominal pressure of as much as 230 MPa.

[6] The low strength of the NaCl confining medium (at 400°C and strain rates as fast as 10^{-4} s⁻¹, NaCl is weaker than 5 MPa [Heard, 1972]) provided a near-hydrostatic state of stress. Our calcite → aragonite transformation experiments confirm this hydrostatic state: Carrara marble undergoes twinning and dislocation glide at stresses as low as 50 MPa at 600°C and a strain rate of 10^{-6} s⁻¹ [Hacker and Kirby, 1993], but we did not observe any evidence of new optical microscope-scale mechanical twins or undulatory extinction in our marble samples, indicating that differential stresses were <50 MPa. Temperature gradients in the assemblies, determined through use of multiple thermocouples, were less than 5°C over the 6 mm sample length.

2.2.1. Equilibrium Experiments

[7] Reversal experiments to establish the position of the calcite-aragonite equilibrium (Figure 1a and Table 1) were conducted to provide a firm foundation for calculating the change in Gibbs free energy during the kinetic experiments. Calcite for the equilibrium experiments was prepared by grinding Carrara marble to a particle size of <20 μm. Aragonite was prepared by transforming the ground calcite at 600°C and 2.20 GPa for 18 hours. Calcite and aragonite were then mixed in equal mass proportions totaling 10–15 mg, reground, and welded inside silver capsules with ~0.3 mg H₂O (~2–3 wt % H₂O). Reversal experiments

Figure 1. Calcite-aragonite phase relations. (a) Calcite ↔ aragonite equilibrium experimental data (triangles, squares, and circles) and conditions of calcite → aragonite transformation experiments (stars). Only the two experiments that define the equilibrium at a given temperature are shown; many additional equilibrium experiments were conducted. The symbols show the maximum possible width of the bracket, determined by the mean pressure of the bracket plus or minus the uncertainty in absolute pressure. The solid line shown is our preferred fit of Johannes and Puhan’s [1971] gas apparatus data at 100–400°C and our experiments at 600–800°C. Two calculated positions for the equilibrium are shown: the pure CaCO₃ system (lower pressure curve) and the Ca_{99.5}Mg_{0.5}CO₃ system (assuming ideal mixing of Ca and Mg in calcite) [Holland and Powell, 1998]. (b) The Ca_{99.5}Mg_{0.5}CO₃ system, based on Irving and Wyllie [1975] and equilibrium experiments in apparatus 1. Dashed lines in the aragonite + calcite field are isopleths of mol % MgCO₃ in calcite and of vol % calcite expected in our samples. Inset shows *T* – *X*_{Mg} relations at 2.5 GPa. Stars show temperatures and nominal pressures of kinetic experiments.

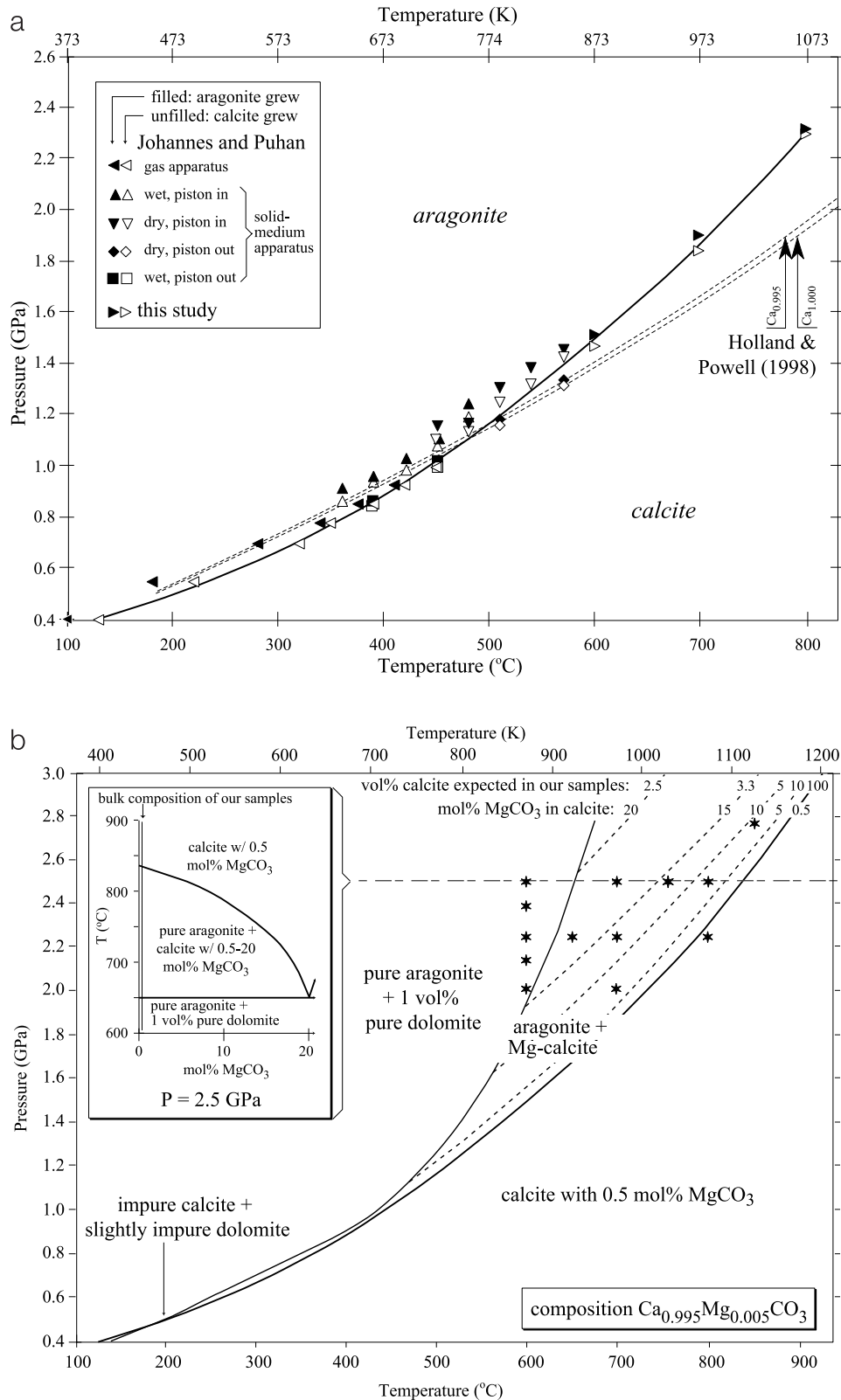


Figure 1

were performed in apparatuses 1 and 2 for 6 to 89 hours at temperatures of 600, 700, and 800°C at pressures of 1.47–2.42 GPa. To reach experimental conditions, each sample was pressurized to ~90% of the final pressure, heated in 5–

10 min to the desired temperature, and then pumped to the final pressure in less than one minute. Quenching at the end of an experiment was achieved by cutting power to the heating element, resulting in cooling to <300°C in <5 s. Run

products were analyzed by X-ray diffraction and by optical microscopy of crushed grains mounted in refractive liquids.

2.2.2. Transformation Experiments

[8] Cylindrical samples 6.4 mm in diameter and 6.4 mm long were drilled from a block of Carrara marble, vacuum dried at 175°C, and welded inside cylindrical silver tubes with flanged endcaps that were formed by pressing through a steel die. Experiments lasted from 15 min to 16 days at temperatures of 500–800°C and pressures of 1.78–2.74 GPa (Figure 1 and Table 2). Experimental conditions in piston cylinder apparatus are normally reached by pressurization at room temperature followed by heating to reach the desired temperature. In an effort to minimize deformation of the samples during runup, we instead pressurized the samples at elevated temperature. After the initial application of ~35 MPa to ensure electrical conduction through the resistive heating system, the temperature was elevated to ~125°C to soften the NaCl confining medium. Temperature and pressure were then increased simultaneously at a rate of ~100 MPa/minute and 50 K/minute until the desired temperature was reached. Then the pressure was increased to the desired value within about 1 minute. Quenching at the end of an experiment was achieved by cutting power to the heating element, resulting in cooling to <300°C in <5 s. The experiment duration, from the time that experimental conditions were reached until the power was turned off, was measured to the nearest second for runs of <1 hour and to the nearest minute for longer runs. The accuracy is poorer, however, because of the time spent increasing pressure within the aragonite stability field before the desired pressure was reached and because of the 5 s required to quench the experiment. At worst, the uncertainty is ±120 s for experiments ≥1 hour and ±65 s for shorter experiments.

[9] The driving force for the reaction was reduction of the Gibbs free energy of the sample, which is approximately the product of an imposed pressure overstep and the volume change (–2.2 to –1.7 cm³/mol at 500 to 850°C). The pressure oversteps were as large as 1.0 GPa (Figure 1 and Table 2), resulting in Gibbs free energy changes ($\Delta_r G$) of as much as –2050 J/mol.

[10] Reaction microstructures were characterized by optical and universal stage microscopy. The presence of aragonite was verified by staining with Feigl's solution [Friedman, 1959], X-ray diffraction, and transmission electron microscopy (TEM). TEM was conducted using Philips 400 (120 keV) and CM20FEG (200 keV) microscopes at Stanford University. Compositions of phases were determined by energy-dispersive analysis (AEM) using CM20 microscopes at Stanford University and at the Bayerisches Geoinstitut (assisted by T. Sharp). For AEM, the accelerating voltage was 200 keV, the spot size was 5, the gun excitation voltage was 4.5 keV, the C1 condenser aperture was 30–50 μm, and the specimen was tilted 20° toward the detector. A live counting time of 90 s was used, with count rates of 1000–2000 s^{–1}. Backgrounds were set manually, and a thin-film approximation was used. Compositions of unknowns were calculated by ratioing background-corrected counts for the unknown to background-corrected counts for adjacent or nearby initial calcite grains whose composition was assumed to match the bulk composition determined by optical spectroscopy. The 1σ precision of the

AEM Mg measurements is ±0.05 wt %, as determined by replicate analyses of the starting material.

3. Results

3.1. Equilibrium Experiments in Pure CaCO₃

[11] Not only is the precise location of the calcite-aragonite equilibrium boundary an important baseline for calculating the Gibbs free difference driving the transformation in our experiments, but the reaction is also widely used to interpret the *PT* histories of high-pressure metamorphic rocks. Experiments to define the calcite-aragonite equilibrium boundary have been conducted by a number of authors (see review by Boettcher and Wyllie [1968]), but most comprehensively by Johannes and Puhani [1971] (Figure 1a). Because pressures are known more accurately in gas apparatus (±20 MPa), the equilibrium boundary at temperatures of 100–450°C is best defined by Johannes and Puhani's [1971] gas apparatus experiments. At pressures greater than those generated in gas apparatus, the solid medium apparatus piston-out experiments ("dry" and "wet") of Johannes and Puhani [1971] define an equilibrium boundary that is consistent with their gas apparatus experiments. We accept these data as the best definition of the calcite-aragonite equilibrium boundary at temperatures of ~400 to 570°C (solid line in Figure 1a).

[12] Not all experimental results agree with this location of the equilibrium boundary, but we exclude those in disagreement for the following reasons. Johannes and Puhani's [1971] "dry" and "wet" piston-in reversal pressures are not equivalent and, moreover, are all ~100 MPa higher than their piston-out experiments. The differences between their piston-in and piston-out experiments must be related to friction between the pressure vessel wall and their NaCl assembly.

3.2. Equilibrium Experiments With 0.5 mol % MgCO₃

[13] The introduction of Mg has a profound effect on equilibrium phase relations in the CaCO₃ system [Irving and Wyllie, 1975]. At temperatures greater than ~400°C, the presence of Mg stabilizes calcite to higher pressure because Mg is partitioned preferentially into calcite relative to aragonite; the Figure 1b inset shows this relation in *T* – *X*_{Mg} space at a pressure of 2.5 GPa. This partitioning produces a cornucopia-shaped, two-phase field where pure aragonite and Mg-bearing calcite coexist. Within this field, the Mg content of calcite is a function of pressure and inverse temperature (dashed line in Figure 1b); at 2.5 GPa, for example, the mole fraction of MgCO₃ stable in calcite rises from 0.5% (the composition of our starting material) at the equilibrium boundary to nearly 20% at ~650°C. Our Carrara marble has 0.5 mol % MgCO₃; therefore the volume fraction of Mg-bearing calcite in equilibrium with aragonite ranges from 100% along the low-pressure boundary of this field where the calcite is Ca_{0.995}Mg_{0.005}CO₃ to 2.5 vol % along the Ca_{0.80}Mg_{0.20}CO₃ isopleth. With increasing pressure and decreasing temperature, impure calcite + aragonite breaks down to pure dolomite + aragonite, which in our system with 0.5 mol % MgCO₃, means 1 vol % dolomite coexisting with 99 vol % pure aragonite.

[14] Reversal experiments in our apparatus 1 define the calcite-aragonite equilibrium at 600–800°C (Table 1 and

Table 2. Calcite → Aragonite Transformation Experiments^a

Experiment	<i>T</i> , K	<i>P</i> , GPa	Time, hours	Reaction	Size, μm	Grain Shape	P_{eq} , GPa	ΔP , MPa	$\Delta_r G$, J mol ⁻¹	Diameter, μm	Spacing, μm	Volume, %
1PC26	773	1.78 + 0.007	24	0%	0	n/a	1.17	610	-1330	n/a		
2PC27	773	1.78 + 0.02	48	0%	0	n/a	1.22	560	-1221	n/a		
1PC4	773	1.70 + 0.004	89	1%	1.7–3.4	rod	1.17	530	-1155	n.v.		
1PC46	873	2.00	4	23%	3.0	rod	1.49	510	-1010	0.5 ± 0.2	1.0 ± 0.5	
1PC56	873	2.00	8	41%	3.4	rod	1.49	510	-1010	0.7 ± 0.2	2.5 ± 0.5	9
1PC18	873	2.00	24	43%	8.5	equant	1.49	510	-1010	n.v.		
1PC1	873	2.00 – 0.014	48	52%	10.0	rod	1.49	510	-1010	n.v.		
1PC2	873	2.00 – 0.018	96	29%	5.1–8.5	rod	1.49	510	-1010	1.0 ± 0.2	3.5 ± 0.5	8
1PC3	873	2.00 – 0.011	192	62%	22.5	rod	1.49	510	-1010	1.2 ± 0.2	3.5 ± 0.5	7
1PC38	873	2.24	1	3%	1.7–3.4	rod	1.49	750	-1538	n.v.		
1PC44	873	2.24	2	22%	1.7–3.4	rod	1.49	750	-1538	n.v.		
1PC45	873	2.24	4	28%	3.0	rod	1.49	750	-1538	n.d.		
2PC37	873	2.24	8	26%	3.5–5.1	rod	1.55	690	-1415	0.3 ± 0.1	1.3 ± 0.2	9
1PC34	873	2.24	24	70%	17–42.5	rod	1.49	750	-1538	0.3 ± 0.2	1.2 ± 0.2	6
1PC31	873	2.24 – 0.011	48	64%	34–51	rod	1.49	750	-1538	0.7 ± 0.2	2.5 ± 0.5	
1PC15	873	2.24 – 0.025	96.05	97%	100	rod	1.49	750	-1538	1.2 ± 0.2	4 ± 1	3
2PC35	873	2.49	1	6%	<1.7	rod	1.55	940	-1927	n.v.		
1PC47	873	2.49	2	25%	5.1	rod	1.49	1000	-2050	n.v.		
1PC49	873	2.49	4	47%	8.5	rod	1.49	1000	-2050	n.v.		
1PC16	873	2.49 – 0.036	24	81%	n.d.	rod	1.49	1000	-2050	0.3 ± 0.1	1.5 ± 0.5	10
1PC12	873	2.49 – 0.07	48	97%	n.d.	rod	1.49	1000	-2050	n.d.		
1PC11	873	2.49 – 0.022	96.08	100%	75	rod	1.49	1000	-2050	0.7 ± 0.2	2.5 ± 0.5	6
1PC25	873	2.49 – 0.014	118.67	100%	100	rod	1.49	1000	-2050	1.0 ± 0.3	3.0 ± 0.5	7
2PC74	923	2.24	0.5	3%	1.0	rod	1.73	510	-1010	n.v.		
2PC102	923	2.24	1	15%	2.5	rod	1.73	510	-1010	0.4 ± 0.1	2.2 ± 0.2	5
2PC103	923	2.24	4	23%	7.5	rod	1.73	510	-1010	0.7 ± 0.2	2.2 ± 0.2	14
2PC80	923	2.24 + 0.002	8	53%	7–10	rod	1.73	510	-1010	0.7 ± 0.2	2.5 ± 0.5	12
2PC105	923	2.24	24	64%	25	rod	1.73	510	-1010	n.d.	3.0 ± 0.5	
2PC106	923	2.24	48	99%	75	rod	1.73	510	-1010	0.7 ± 0.1	3.0 ± 0.3	8
2PC104	923	2.24	96	100%	75	rod	1.73	510	-1010	1.1 ± 0.2	3.0 ± 0.5	9
1PC68	923	2.24	1	17%	2.0	rod	1.66	580	-1148	0.7 ± 0.2	3.5 ± 1.5	8
1PC72	923	2.24	2	14%	1.0	rod	1.66	580	-1148	0.7 ± 0.3	2.5 ± 1	
1PC61	923	2.24 + 0.027	48	25%	2–5	rod	1.66	580	-1148	1.5 ± 0.5	4 ± 1	9
1PC59	923	2.24 – 0.013	95.33	36%	7.5–12.5	rod	1.66	580	-1148	1.5 ± 0.5	4 ± 1	11
2PC30	973	2.00	24	0%	0.0	n/a	1.94	60	-115	n/a		
2PC32	973	2.00 – 0.007	96	27%	10.2–17	equant	1.94	60	-115	rare		
1PC43	973	2.00 – 0.007	192	0%	0.0	n/a	1.87	130	-248	n/a		
2PC71	973	2.24	0.25	9%	1.0	rod?	1.94	300	-573	n.v.		
2PC69	973	2.24	0.5	0%	0.0	n/a	1.94	300	-573	n/a		
1PC113	973	2.24	0.25	5%	1.5	rod?	1.87	330	-630	0.5 ± 0.2	2.0 ± 0.5	20
1PC114	973	2.24	0.5	22%	2.5	rod	1.87	330	-630	0.7 ± 0.1	2.0 ± 0.5	17
1PC39	973	2.24	1	35%	5.1–8.5	rod	1.87	330	-630	1.0 ± 0.2	2.5 ± 0.5	17
1PC53	973	2.24	2	46%	6.8	rod	1.87	330	-630	1.2 ± 0.2	3 ± 1	12
1PC54	973	2.24	4	76%	20	rod	1.87	330	-630	1.2 ± 0.2	2.5 ± 0.5	14
1PC40	973	2.24	8	55%	17	rod	1.87	330	-630	1.5 ± 0.5	3 ± 1	15
1PC9	973	2.24 – 0.011	24	77%	50	rod	1.87	330	-630	1.5 ± 0.5	3 ± 1	9
1PC6	973	2.24 – 0.029	46.5	85%	100	rod	1.87	330	-630	1.4 ± 0.3	3 ± 1	4
1PC5	973	2.24 – 0.18	95	100%	100	rod	1.87	330	-630	1.0 ± 0.2	4 ± 1	7
1PC20	973	2.24 – 0.04	192.75	100%	100	rod	1.87	330	-630	1.5 ± 0.3	3 ± 1	8
2PC75	973	2.49	0.55	0%	0.0	n/a	1.94	550	-1051	n/a		
2PC36	973	2.49	1	52%	17–34	rod	1.94	550	-1051	0.5 ± 0.3	2 ± 0.5	17
1PC70	973	2.49	0.25	19%	1.0	rod	1.87	620	-1184	n.v.		
1PC112	973	2.49	0.5	25%	5.0	rod	1.87	620	-1184	0.3 ± 0.1	2 ± 0.2	14
1PC111	973	2.49	1	27%	7.5	rod	1.87	620	-1184	0.6 ± 0.1	2 ± 0.2	18
1PC48	973	2.49	2	41%	5.1	rod	1.87	620	-1184	0.4 ± 0.1	2.0 ± 0.5	14
1PC55	973	2.49	4	92%	65	rod	1.87	620	-1184	0.7 ± 0.2	2 ± 0.5	12
1PC52	973	2.49	8	98%	100	rod	1.87	620	-1184	0.7 ± 0.2	2.0 ± 0.5	11
1PC17	973	2.49 – 0.014	24.02	100%	100	rod	1.87	620	-1184	0.7 ± 0.2	2.5 ± 0.5	9
1PC14	973	2.49 – 0.029	48	100%	100	rod	1.87	620	-1184	0.8 ± 0.2	4 ± 1	12
1PC13	973	2.49 – 0.032	96	100%	100	rod	1.87	620	-1184	1.4 ± 0.3	2.5 ± 0.5	10
1PC24	973	2.49 – 0.029	191.67	100%	100	rod	1.87	620	-1184	1.3 ± 0.3	3 ± 1	11
2PC76	1023	2.49	1	25%	2–5	rod	2.15	340	-626	0.9 ± 0.2	2.5 ± 0.5	15
2PC78	1023	2.49	2	52%	10.0	rod	2.15	340	-626	1.1 ± 0.2	2.5 ± 0.5	18
2PC77	1023	2.49	4	45%	10–20	rod	2.15	340	-626	1.0 ± 0.2	3.0 ± 0.5	18

Table 2. (continued)

Experiment	T , K	P , GPa	Time, hours	Reaction	Size, μm	Grain Shape	P_{eq} , GPa	ΔP , MPa	$\Delta_r G$, J mol $^{-1}$	Diameter, μm	Spacing, μm	Volume, %
2PC81	1023	2.49	8	74%	25	rod	2.15	340	-626	1.2 ± 0.3	3.0 ± 0.5	12
2PC64	1023	2.49 - 0.007	24	100%	50-100	rod	2.15	340	-626	1.5 ± 0.5	4.0 ± 1.0	10
2PC41	1073	2.24 - 0.15	96	34%	10.2	equant	2.49	-250	+443	n.v.		
1PC42	1073	2.24 + 0.029	192	0%	0?	n/a	2.31	-70	+124	n/a		
2PC79	1073	2.49 - 0.014	3.83	0%	0.0	n/a	2.49	0	0	n/a		
1PC67	1073	2.49	1	14%	1.0	equant	2.31	180	-319	n.v.		
1PC51	1073	2.49	2	29%	1.7-3.4	equant	2.31	180	-319	n.v.		
1PC58	1073	2.49 + 0.007	4	38%	5.1	equant	2.31	180	-319	n.v.		
1PC57	1073	2.49	8	45%	6.8	equant	2.31	180	-319	n.v.		
1PC10	1073	2.49 - 0.022	24	47%	10.2	mixed	2.31	180	-319	1.5	>10	<1
1PC7	1073	2.49 - 0.018	48	63%	13.6-17	equant	2.31	180	-319	0.1	1	1
1PC8	1073	2.49 - 0.025	96.02	72%	17	equant	2.31	180	-319	n.v.		
1PC22	1073	2.49 - 0.025	192	38%	10.2-13.6	equant	2.31	180	-319	n.v.		
4PC84	1123	1.90	4	0%	n/a	n/a	2.54	200	-340	n/a		
4PC86	1123	2.74	8	72%	50-75	rod	2.54	200	-340	0.8 ± 0.1	2.2 ± 0.2	11, 16, 25

^aFirst digit of each experiment number identifies either apparatus 1 or 2 was used for the experiment. Size is width or diameter of reaction zones; P is gauge pressure, number following is maximum deviation observed during experiment; P_{eq} is apparent equilibrium pressure at this temperature as determined from equilibrium experiments in the same apparatus (except for 773 K, which is extrapolated); for uncertainties, see parenthetical numbers in Table 1; ΔP is difference between run pressure and equilibrium pressure (uncertainty is ~ 30 MPa); $\Delta_r G$ is change in Gibbs free energy approximated as $dP\Delta_r V$ from THERMOCALC [Powell *et al.*, 1998]; diameter is diameter of calcite inclusions; spacing is spacing between calcite inclusions; volume is volume fraction of calcite inclusions within aragonite; n.d. is not determined because of poor thin section; n.v. indicates that inclusions are not visible because they are small or absent.

Figure 1a), based on changes from our starting mix of 50 wt % calcite + 50 wt % aragonite. Our apparatus 2 results lie at 60–80 MPa higher pressure (Table 1) but within the ± 70 MPa uncertainty for each apparatus. As discussed earlier, the relative uncertainty among experiments in a single apparatus is ~ 30 MPa, so these P brackets have an uncertainty of ~ 30 MPa + the half width of the bracket, or 1.49 ± 0.05 GPa at 600°C, 1.87 ± 0.06 GPa at 700°C, and 2.31 ± 0.04 GPa at 800°C for apparatus 1. The uncertainty in the absolute pressures of these reversals is ± 70 MPa plus the half width of the bracket, or 1.49 ± 0.09 GPa, 1.87 ± 0.10 GPa, and 2.31 ± 0.08 GPa, respectively. The presence of Mg means that these reversals do not strictly apply to the calcite-aragonite equilibrium in the pure CaCO_3 system. However, the equilibrium we reversed, $\text{Ca}_{99.5}\text{Mg}_{0.5}\text{CO}_3$ calcite = Mg-calcite + pure aragonite (between the 10 and 100 vol % curves in Figure 1b), should differ from the pure system by less than 30 MPa (calculated using THERMOCALC [Powell and Holland, 1988]), within our absolute pressure uncertainty.

[15] Our solid medium apparatus 1 experiments are in reasonable agreement with Johannes and Puhan's [1971] gas apparatus and piston-out experiments given that probable ~ 70 MPa inaccuracy for the piston-cylinder brackets of Johannes and Puhan [1971]. If we include the theoretical 298 K equilibrium pressure of 0.299 GPa calculated by Königsberger *et al.* [1989] on the basis of their measurements of $\Delta_r G^\circ$ and $\Delta_r S^\circ$, all the gas apparatus data and our new high-pressure data can be fit by the equation: P (GPa) = $2.4 \times 10^{-6} * (T - 298)^2$ (K) - $7.4 \times 10^{-4} * (T - 298)$ (K) + 0.299, indicated by the solid line in Figure 1a.

[16] The curvature of the equilibrium boundary in PT space is largely related to rotational disorder of CO_3 groups as calcite changes gradually from the $R\bar{3}c$ to the $R\bar{3}m$ space group with increasing temperature [Carlson, 1983]. The

excess entropy associated with this ordering continually increases up to a temperature of $987 \pm 5^\circ\text{C}$, above which disordering is complete [Dove and Powell, 1989; Redfern *et al.*, 1989]. The position of the reaction calculated using THERMOCALC [Powell and Holland, 1988] is shown with a dashed line in Figure 1a. Our piston-cylinder experiments suggest that the entropy change calculated by THERMOCALC may be too low.

3.3. Transformation Experiments

[17] The transformation of calcite to aragonite varied in our experiments from 0% to 100% for timescales of minutes to days at the experimental pressures and temperatures of this study (Figure 1). We were able to quench microstructures of partial transformation at different PT conditions, at different extents of reaction, and at different observational scales. We were also able to measure the nucleation rates, growth rates and overall transformation rates at different physical conditions.

[18] Calcite crystals recovered from samples that did not transform to aragonite show minor differences from the starting material, a lower dislocation density (10^{11} – 10^{12} m $^{-2}$) and less tangling of the dislocations (Figure 2a), suggesting that some recovery occurred during the experiments. This observation is consonant with observations of widespread dislocation climb at temperatures above 600°C in deformation experiments on Carrara marble [e.g., Hacker and Kirby, 1993].

[19] Aragonite neoblasts are found predominantly on calcite/calcite grain boundaries (Figure 2b); fewer than 1% of the neoblasts occur on intracrystalline defects such as dislocations and twins. The restriction of aragonite neoblasts to grain boundaries is expected in a solid rock, because grain boundary free energies are larger than the free energies of intragranular defects [Gilman, 1960; Murr,

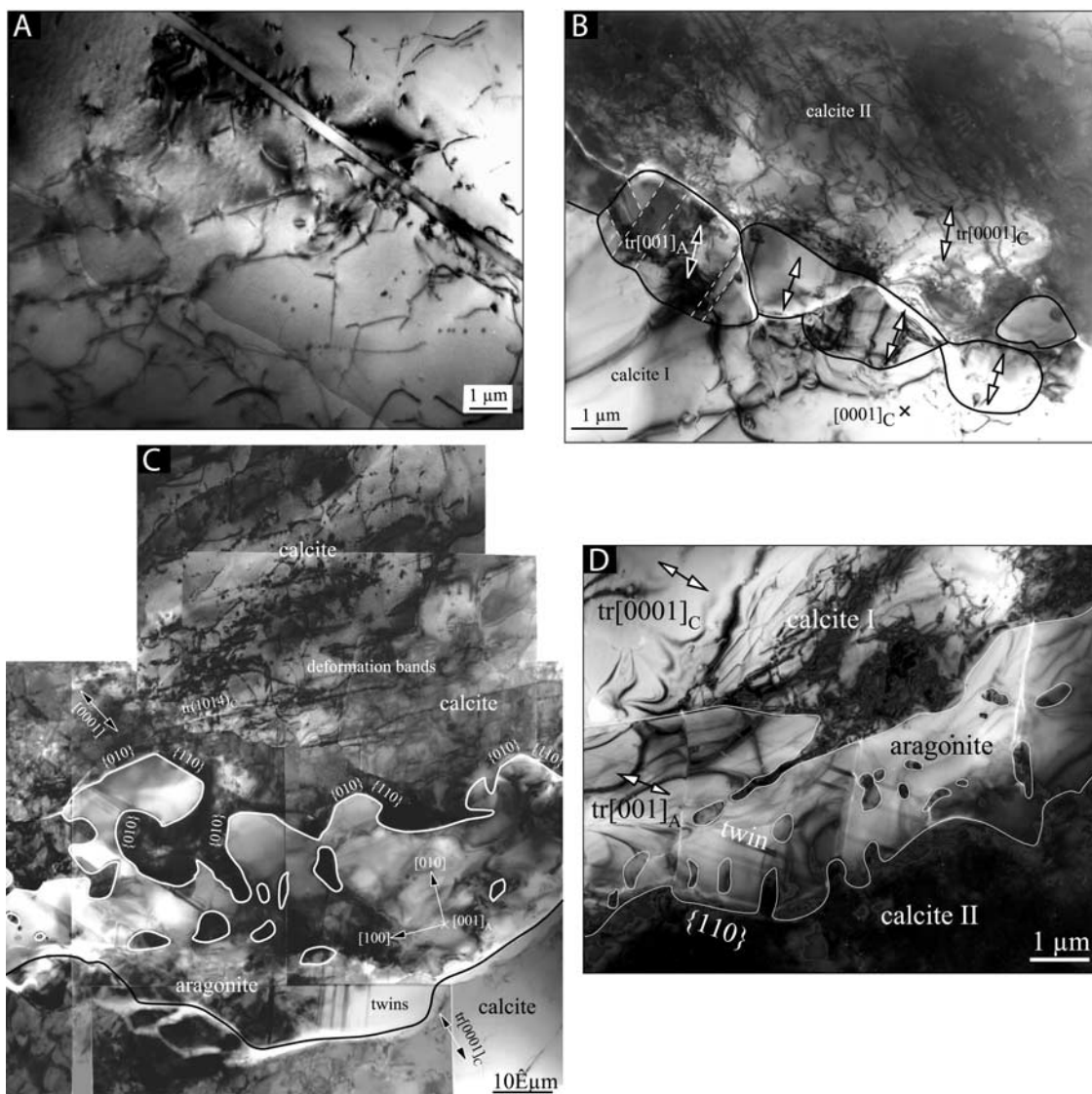


Figure 2. Early stages of the calcite → aragonite transformation seen with transmission electron microscopy (sample IPC38 transformed 3% in 1 hour at 600°C and 2.24 GPa). (a) Host calcite crystal shows curved unit and networked dislocations in densities of 10^{11} – 10^{12} m^{-2} , with minor twins and small bubbles or solid inclusions. (b) Five small (1–2 μm) aragonite neoblasts that have slight misorientations with respect to each other and are topotactic with adjacent calcite crystal II. Traces of aragonite c axes, $[001]_A$, and calcite c axes, $[0001]_C$, within the plane of the foil are shown with double-headed arrows; $[001]_A$ varies slightly from subgrain to subgrain, but all are subparallel to $(0001)_C$ in the upper host calcite grain. Twins within one aragonite grain are indicated with dashed lines. Dislocations in the host calcite are more rectilinear than in Figure 2a. (c) Faceted prongs of twinned aragonite growing into a host calcite crystal that contains a high density of defects. Rods and blebs of calcite are present down to sizes less than 30 nm. Host calcite grain at top contains an increasing density of increasingly rectilinear dislocations in the vicinity of the aragonite crystal. Rectilinear zones parallel to the trace of $\{10\bar{1}4\}_C$ are slip bands or healed cracks. (d) Reaction zone with twinned aragonite shows a diagonal calcite rod clearly formed from calcite crystal I and calcite relicts of many sizes, some of which are clearly related to each of the visible calcite crystals. The interface marked $\{110\}$ is subparallel to the trace of the $\{110\}$ aragonite twins.

1975], which constitute the only other probable nucleation site. Aragonite neoblasts visible with optical microscopy are generally of similar size and coat all grain boundaries, implying that nucleation occurred chiefly during the early

stages of the experiments, rather than occurring continuously over the duration of the experiments.

[20] Two different textures, termed “rod” or “equant” (or “mixed”, if the texture was intermediate) in Table 2 were

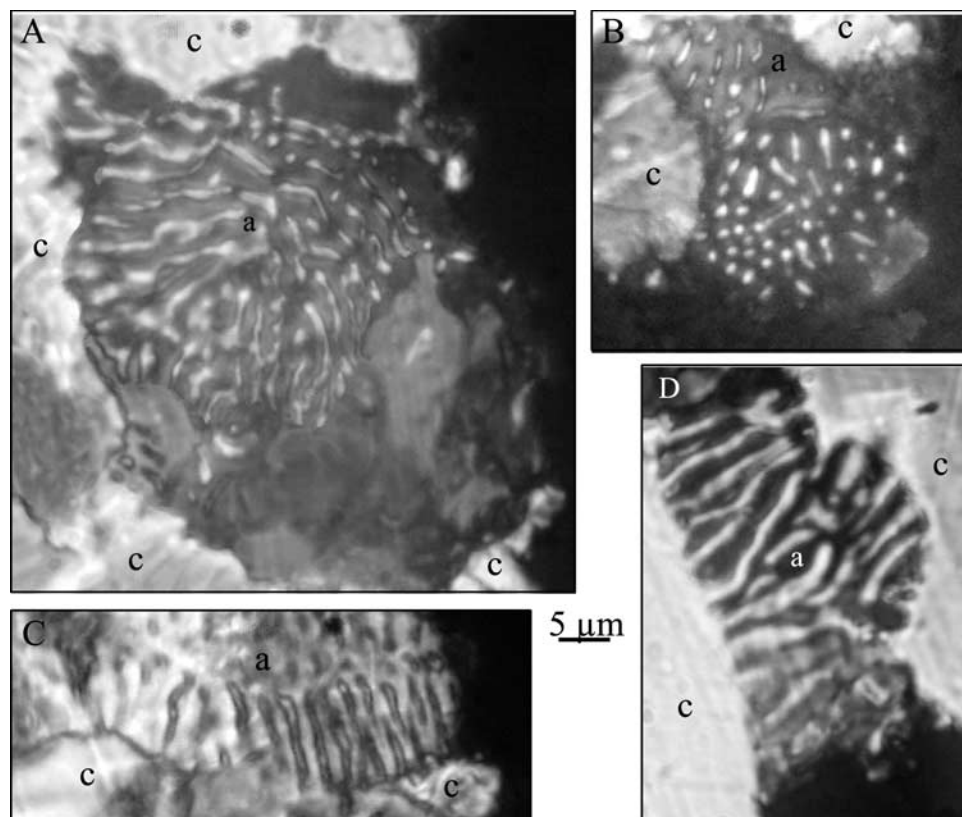


Figure 3. Intermediate stages of the calcite → aragonite transformation seen in polarized, transmitted light micrographs of ultrathin sections. (a, b) PC106 transformed 99% in 48 hours at 650°C and 2.24 GPa. (c) PC86 transformed 72% in 2 hours at 850°C and 2.74 GPa. (d) PC78 transformed 52% in 2 hours at 750°C and 2.49 GPa; c, calcite starting material; a, aragonite. Rod-like objects in the transformed material are high-Mg calcite inclusions; many of those rods are viewed end on in Figure 3b.

produced in the experimental samples. Sections 3.3.1–3.3.3 describe these two textures using TEM, optical microscopy, and electron probe microanalysis.

3.3.1. Rodlike Textures

[21] Study of ultrathin ion-milled sections by optical microscopy and transmission electron microscopy shows that the transformation began with the development of aragonite grains on the calcite grain boundaries, and ended with aragonite grains up to 100 μm diameter containing numerous ~1-μm-diameter calcite rods (Figures 2 and 3). As detailed below, the rodlike texture resulted from the partitioning of the Mg from the starting material into Mg-rich calcite rods in Mg-poor aragonite host, as expected from the phase relations (Figure 1b).

[22] The earliest stages of reaction visible with the optical microscope show aragonite grains that are 1–2 μm thick (perpendicular to their host calcite grain boundaries) and 5–30 μm wide along the calcite/calcite grain boundaries. TEM shows an earlier stage of 1–2 μm diameter neoblasts that are misoriented with respect to each other by a few degrees and tightly spaced along calcite grain boundaries (Figure 2b). These aragonite neoblasts are not strongly faceted but have curvilinear boundaries. They are nearly free of internal defects, other than containing occasional twins; however, adjacent host calcite grains have elevated dislocation densities of 10^{12} – 10^{13} m⁻² (compare Figures 2a and 2b). Neither TEM nor optical microscopy reveal

calcite rods within these early formed 1–2 μm aragonite neoblasts.

[23] Most experimental studies of transformations between calcite and aragonite have observed a topotactic relation between the two phases, in which the *c* axes of aragonite and calcite are subparallel [e.g., *Carlson and Rosenfeld*, 1981]. Selected area electron diffraction reveals that the aragonite neoblasts in Figure 2b have *c* axes, $[001]_A$, subparallel to *c* in one of the adjacent calcite crystals, $[0001]_C$. Each of the aragonite grains is slightly misoriented with respect to the others and to the host calcite by up to 5° rotation about an axis parallel to $\sim[100]_A$; in other words, the aragonite *c* axes are not exactly parallel to $[0001]_C$. Not every aragonite crystal that we examined in TEM has an obvious topotactic relationship with adjacent visible calcite grains, but this may be because the crystallographically related calcite crystal is not in the plane of the section.

[24] The interfaces along which the aragonite has grown into the host calcite range from curvilinear to faceted: in Figure 2c, prongs of aragonite with $\{010\}_A$ and $\{110\}_A$ facets have advanced into an adjacent calcite crystal. As noted earlier, aragonite grains contain few dislocations and only a moderate density of twins (Figure 2d). Calcite, however, shows a progressive increase in dislocation density ($>10^{13}$ m⁻²) and deformation bands approaching the aragonite (Figure 2c). These deformation bands are parallel to the

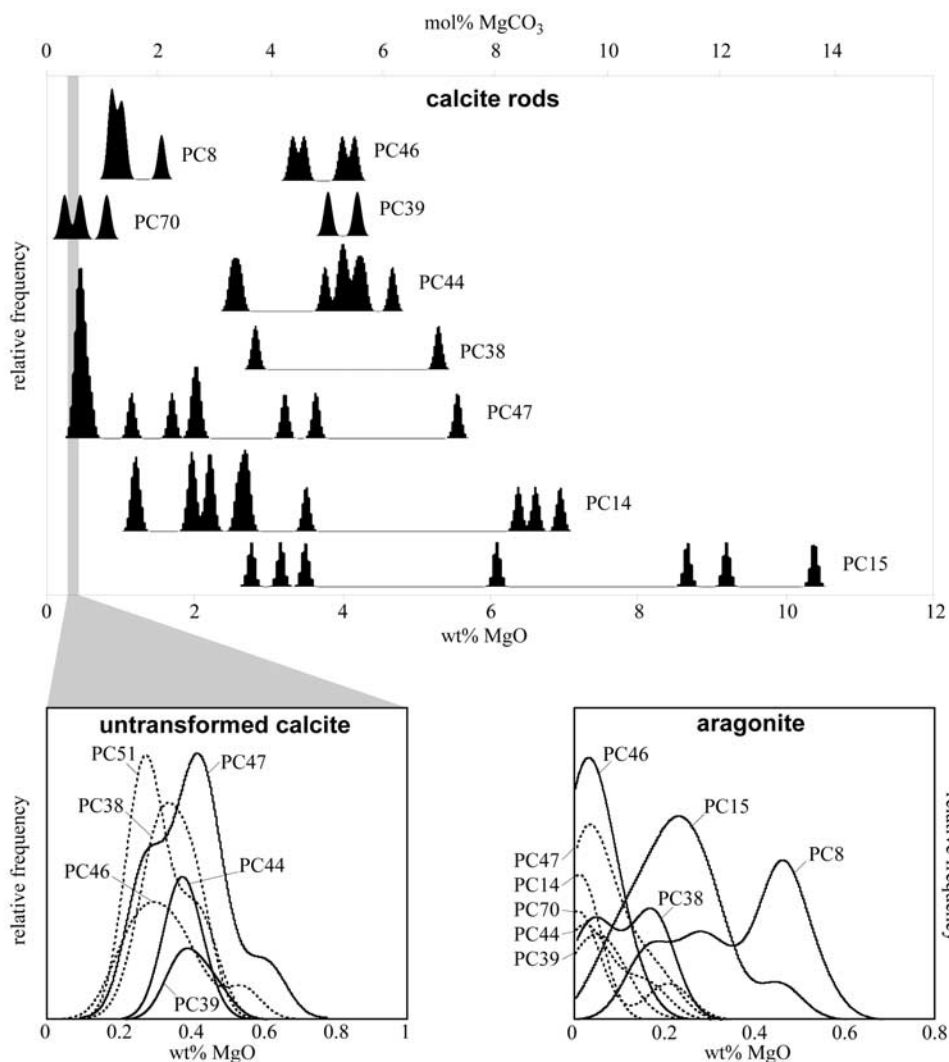


Figure 4. MgO contents determined by analytical electron microscopy. Untransformed calcite is ~ 0.4 wt %, new aragonite grains are generally < 0.4 wt %, and calcite inclusions are enriched to > 10 wt %. “PCxx” numbers refer to experimental sample number. Relative frequency was determined by summing Gaussian distributions of the measured values and their uncertainties.

trace of $\{10\bar{1}4\}_C$, a common slip plane in calcite [Wenk, 1985], and may be modified twins or dislocation arrays.

[25] Aragonite grains that have grown larger than a few microns show intergrowths of Mg-enriched calcite. Optical microscopy and TEM reveal that most of these inclusions are rod shaped and crystallographically continuous with nearby partially consumed calcite crystals (Figures 2c and 2d). In Figure 2d, for example, the aragonite has partially consumed both adjacent calcite crystals: the diagonal, $3\text{-}\mu\text{m}$ -long rod in the middle of the image clearly belongs to the upper calcite crystal, and the lower calcite crystal has its own rods protruding subvertically into the aragonite.

[26] Viewed with the optical microscope (Figure 3), the calcite rods are curved in three dimensions. The long axes of the rods are typically subperpendicular to the reaction front, regardless of the shape of the aragonite grain. Thus, in aragonite grains that bulge into partially consumed calcite grains, the curves of the rods track the path of the reaction front and the rods branch or multiply in such a way that their diameter and spacing are constant (e.g., Figure 3a).

The rods are equant in cross section and, in the optical microscope, range in diameter from 0.3 to $1.7\ \mu\text{m}$ (Figure 3b). Smaller rods are visible with TEM down to the scale of $< 50\ \text{nm}$ (Figure 2d). Rod sizes are relatively constant within individual samples, with a typical range of $\pm 0.2\ \mu\text{m}$. The spacing between rods (measured as the distance from the center of one rod to the next) is also reasonably consistent within single samples (Table 2). As discussed below, both rod diameter and spacing are a function of temperature and the Gibbs free energy change of reaction. The volume fraction of calcite rods present within a single sample varies by about a factor of 2 from grain to grain (see Figure 3 and Table 2).

[27] Samples that appear to have transformed completely to aragonite at the optical scale actually consist of $\sim 50\text{--}70\ \mu\text{m}$ diameter subgrains bearing many calcite inclusions that range in size from $0.1\text{--}1.0\ \mu\text{m}$. These Mg-calcite intergrowths contain high densities of dislocations, and most are surrounded by twins that radiate outward into the aragonite.

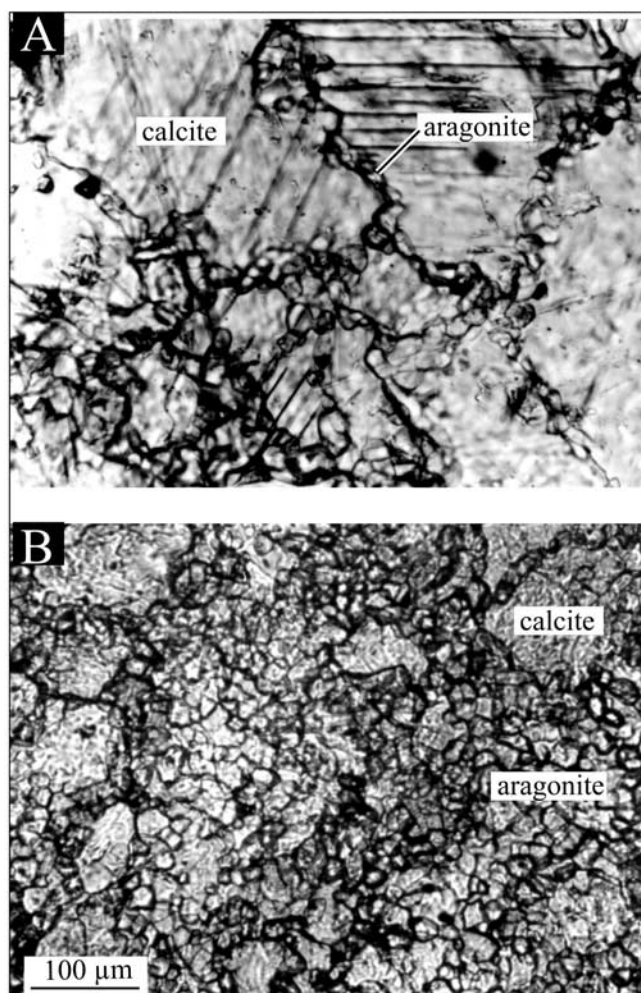


Figure 5. Equant aragonite crystals without included calcite rods grew at temperatures $\geq 800^\circ\text{C}$ (transmitted light micrograph). (a) Early stage of transformation; sample 1PC10 transformed 47% in 24 hours at 800°C and 2.49 GPa. (b) Later stage of transformation; sample 1PC8 transformed 72% in 96 hours at 800°C and 2.49 GPa.

3.3.2. Mg Contents

[28] The calcite grains in the starting material contain, on average, 0.36 wt % MgO (Figure 4, bottom left). Analytical electron microscopy reveals that in all analyzed samples, the aragonite grains contain even less MgO, typically <0.3 wt %, and frequently <0.1 wt % (Figure 4, bottom right). In contrast, the concentration of MgO in the calcite rods is commonly 2–5 wt % (3–7 mol % MgCO_3), and in some grains exceeds 9–10 wt % (12–13 mol % MgCO_3). In one sample it was observed that the MgO concentration of the calcite rods varies inversely with the volume fraction of the rods. Submicron-scale compositional scans conducted with AEM did not reveal gradients in MgO concentration in the unreacted calcite, in the calcite rods, or in the aragonite neoblasts.

3.3.3. Equant Textures

[29] The preceding textural description applies to most samples, but a smaller subset of samples developed a different texture labeled “equant” in Table 2. These textures

developed exclusively in samples with small changes in Gibbs free energy. Samples with small amounts of reaction contain subsequent neoblasts of aragonite spaced about $3\ \mu\text{m}$ apart along the original calcite/calcite grain boundaries (Figure 5a). In other samples, the aragonite crystals have grown and consumed all the calcite crystals (Figure 5b). These equant aragonite grains have 120° triple junctions, planar grain boundaries, and few visible dislocations.

[30] Calcite inclusions in these equant aragonite grains are visible with optical microscopy in only two samples (Table 2). A single “equant” textured sample (PC8) examined by AEM showed partitioning of MgO between the aragonite and calcite, with the calcite inclusions exhibiting lower MgO contents relative to the rod-textured samples and the aragonite grains showing enriched MgO contents relative to the rod-textured samples (Figure 4); that is, the MgO partitioning is not as extreme in the equant texture samples as it is in the rod texture samples.

3.3.4. Nucleation Rates

[31] The minimum grain boundary nucleation rate was measured by counting the number of aragonite grains per host calcite grain in the shortest experiments. At temperatures of 500 – 750°C , the nucleation rate was $>10^7$ nuclei $\text{m}^{-2}\ \text{s}^{-1}$. The equant aragonite crystals that formed at temperatures of 800 – 850°C nucleated at a rate of $>5 \times 10^4$ nuclei per square meter of grain boundary per second.

3.3.5. Growth Rates

[32] The growth rate of the aragonite grains was determined by plotting the measured widths of aragonite grains whose calcite inclusions lie in the plane of the thin section as a function of time (Table 2). The width measurements have an uncertainty of $\sim 10\%$ because of variation among grains and the curvature of the calcite inclusions; samples that exhibit a range of grain sizes are noted in Table 2. Figure 6 shows that the growth rate for the “rod” textured samples does not vary significantly with time or width, and ranges from $\sim 3 \times 10^{-11}\ \text{m}\ \text{s}^{-1}$ at 600°C to $\sim 9 \times 10^{-9}\ \text{m}\ \text{s}^{-1}$ at 850°C . The growth rate for the “equant” textured samples is logarithmic (i.e., exponential in $-1/t$) with time. A mean growth rate for each of the data sets was computed with the program Isoplot [Ludwig, 2001], using measurement errors on experiment duration and grain size as inputs. None of the fits are “good” from a statistical perspective (they have unacceptably high mean sums of weighted deviates), indicating that factors other than experiment duration affected the grain sizes. Most probable culprits are intrarun fluctuations in P and T and intersample variations in initial grain size or impurities. The uncertainties shown in the growth rates for each data set represent 95% confidence intervals. The apparent activation enthalpy of the growth rate was determined to be $166 \pm 91\ \text{kJ}\ \text{mol}^{-1}$ (95% confidence interval) by fitting $\ln \dot{x}/T(1 - \exp[-\Delta_r G/RT])$ to $1/T$ [after Turnbull, 1956], using Isoplot, uncertainties in growth rates as shown in Figure 6, and fixed uncertainties of $\pm \Delta_r G = 200\ \text{J}\ \text{mol}^{-1}$ and $\pm T = 5\ \text{K}$ (Figure 7).

3.3.6. Temporal Changes in Inclusion Textures

[33] The calcite inclusions underwent textural changes over time. Figures 8a and 8d show that the volume fraction of the inclusions is lowest at low temperatures and highest at high temperatures and also decreased logarithmically with time in each data set (Figure 8; except for the

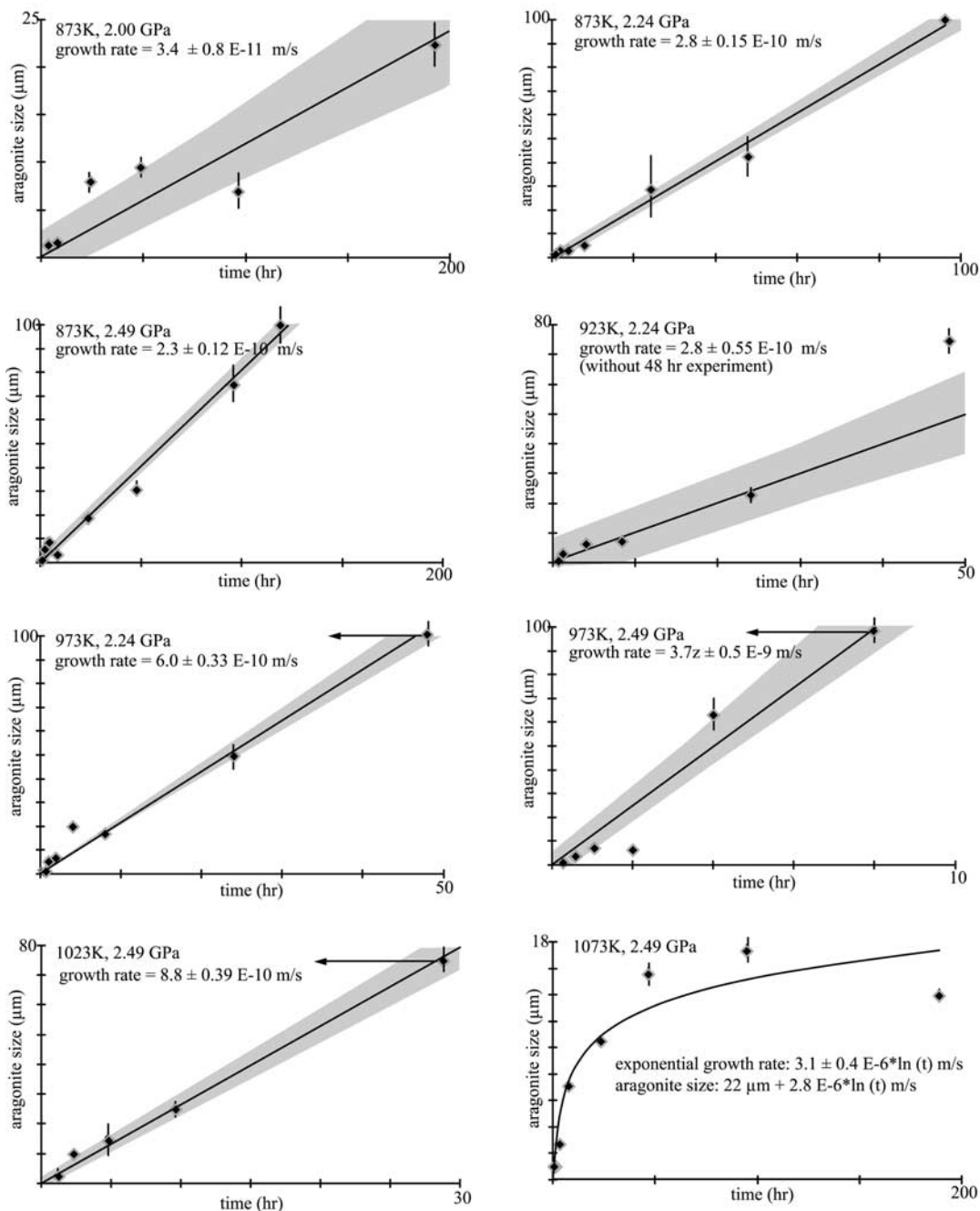


Figure 6. Growth of aragonite from calcite is approximately linear at temperatures of 873–1023 K and exponential at 1073 K.

“923 K, 2.2 GPa, 1” data set). The sizes, D (Figures 8b and 8e) and spacings, λ , (Figures 8c and 8f) of the calcite inclusions also show temporal trends, with larger and more widely spaced inclusions produced in longer experiments. Linear fits to the size versus time and spacing versus time data shown in Figure 8 were computed using a Monte Carlo style method based on a least squares minimization of 10,000 randomly chosen Gaussian-distributed values. The slopes of the $D - \ln t$ fits are not grossly dissimilar and indicate that for all experimental conditions the inclusions increased logarithmically in diameter with time. Three samples, from short experiments of 0.25, 2, and 8 hours,

showed no calcite inclusions within the aragonite grains. Fits to at least two sets of data intersect the ordinate at 0.6–0.8 μm , implying that the first calcite inclusions trapped were of this size.

3.3.7. Transformation Rates

[34] The extent of reaction was determined by counting 400 points in each thin section with an automated point-counting stage on an optical microscope (Figure 9). The precision of this technique is about one percentage point as determined by replicate counts of the same sample. When we began this experimental investigation we were concerned that transformation might begin at the sample surfaces,

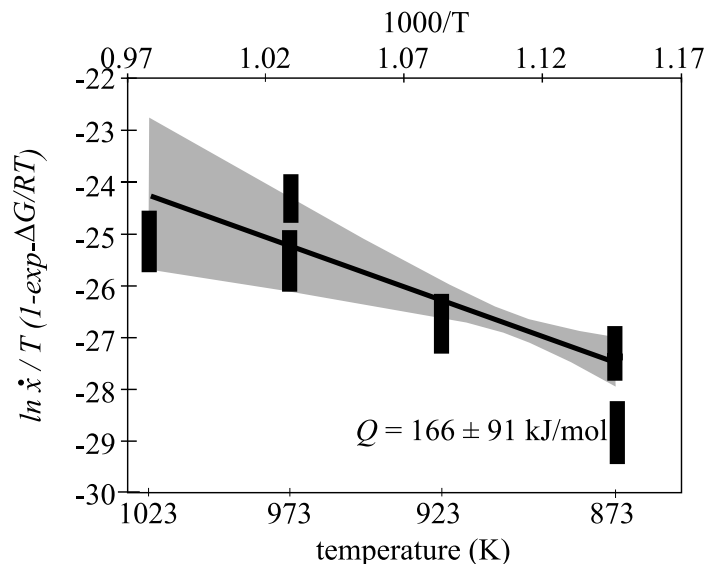


Figure 7. Apparent activation enthalpy for growth of aragonite at temperatures of 873–1023 K is 166 ± 91 kJ/mol when fitted to an equation of the form $\dot{x} = b(kT/h)\{\exp(-Q/RT)[1 - \exp(-\Delta_r G/RT)]\}$ where \dot{x} is growth rate, b an empirical constant, k Boltzmann’s constant, h Planck’s constant, Q the activation energy for growth, $\Delta_r G$ the Gibbs free energy change of reaction, and T temperature [Turnbull, 1956].

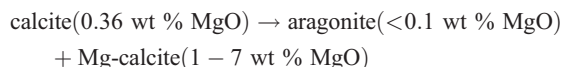
where the surface and defect free energies are likely to have been higher; such behavior was observed by *Rubie and Champness* [1987] in their study of Mg_2GeO_4 olivine \rightarrow spinel. In a few samples, such a shell of aragonite did form, but those few samples were easily identified and discarded. As expected, the reaction was faster at higher temperatures and at higher values of $\Delta_r G$ (i.e., at higher pressure oversteps at a given temperature). The lack of an incubation stage in the transformation rate data is consistent with the textural observation of early nucleation on all grain boundaries and suggests that aragonite nucleation is not the rate-limiting step in this transformation.

4. Discussion

[35] On the basis of the phase relations shown in Figure 1b, samples transformed at 600°C should have formed an equilibrium assemblage of 99 vol % pure aragonite and 1 vol % pure dolomite. Samples transformed at increasingly higher temperatures should have formed an equilibrium assemblage of pure aragonite coexisting with increasing volume fractions of calcite with decreasing amounts of Mg. In contrast to this expectation, our transformed samples contain 3–20 vol % calcite inclusions and no dolomite. The volume fraction of calcite inclusions in our experiments (Figure 8) are also always larger than expected and poorer in Mg than expected (Figure 3). That the volume fractions of calcite inclusions decreased logarithmically with time (Figure 8) suggests that they were approaching, but had not reached, equilibrium. The observation that the inclusions increased in size and spacing over time suggests *Ostwald* [1897] ripening, wherein larger grains grow at the expense of smaller grains. These quantitative changes in texture, combined with the qualitative evolution depicted in Figures 2 and 3, reveal that as the aragonite grains grew, Mg rejected by the aragonite was forced to remain in or diffuse to the calcite. This stabilized

relict calcite inclusions that were trapped in the aragonite crystals by passage of the reaction front. After entrapment, many of the inclusions were cannibalized, and their Mg was incorporated into the remaining inclusions, which grew in diameter and Mg content.

[36] Unquestionably the most unusual, yet characteristic, aspect of these reaction textures is the presence of calcite rods in the transformed material. The reaction observed,



is similar to a cellular precipitation reaction, $\alpha \rightarrow \alpha' + \beta$, wherein a reactant phase α decomposes to form one product phase β with a structure that is entirely new and one phase α' that has the same crystal structure but typically a different crystallographic orientation and composition from the parent phase [Sundquist, 1973]. (“Eutectoid” reactions, $\gamma \rightarrow \alpha + \beta$, involving the breakdown of a single phase to two (or more) phases, neither of which shares the structure or composition of the starting material, are a more general type of decomposition reaction [Spencer and Mack, 1962].) The textural and compositional information detailed above make it clear that the presence of Mg in our starting material, and the fact that aragonite does not admit much Mg into its structure (Figure 1), caused the calcite \rightarrow aragonite transformation to be a cellular precipitation reaction.

4.1. Phenomenology

[37] Eutectoid and cellular precipitation textures form when the reaction interface propagates faster than the diffusing species can “escape” the reaction zone and diffuse to make their own coarse grains, in this case dolomite or Mg-enriched calcite. The spacing of the inclusions that results depends chiefly on the relative volumes of the phases, the rate at which the phases nucleate and grow, the interfacial and strain free energies, the Gibbs free energy

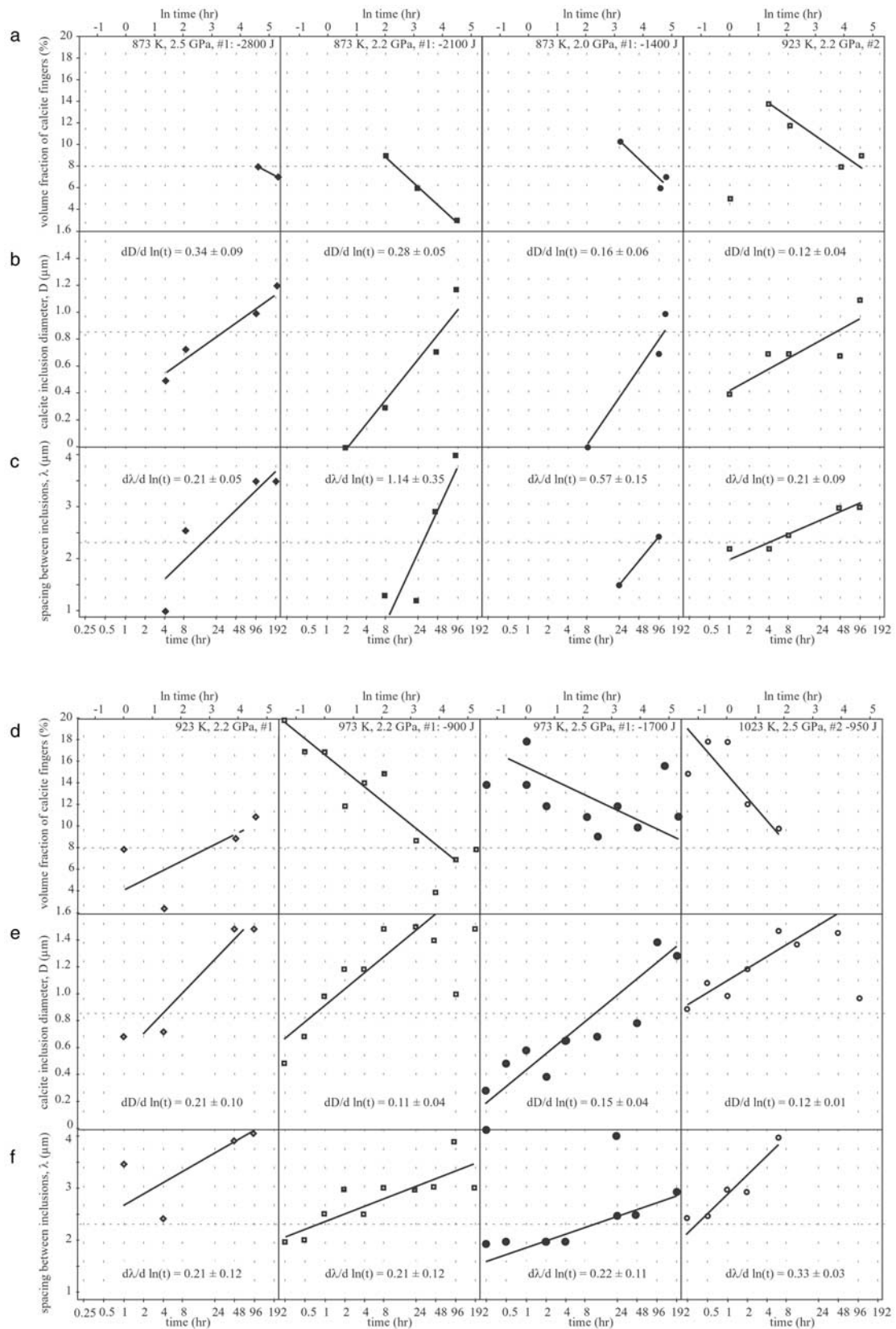


Figure 8. Textural changes in calcite inclusions versus logarithm of time. (a, d) Volume fraction of calcite inclusions is lowest at low temperatures and highest at high temperatures and increased logarithmically with time. (b, e) Diameter of calcite rods increased logarithmically with time. (c, f) Spacing between calcite inclusions increased exponentially with time.

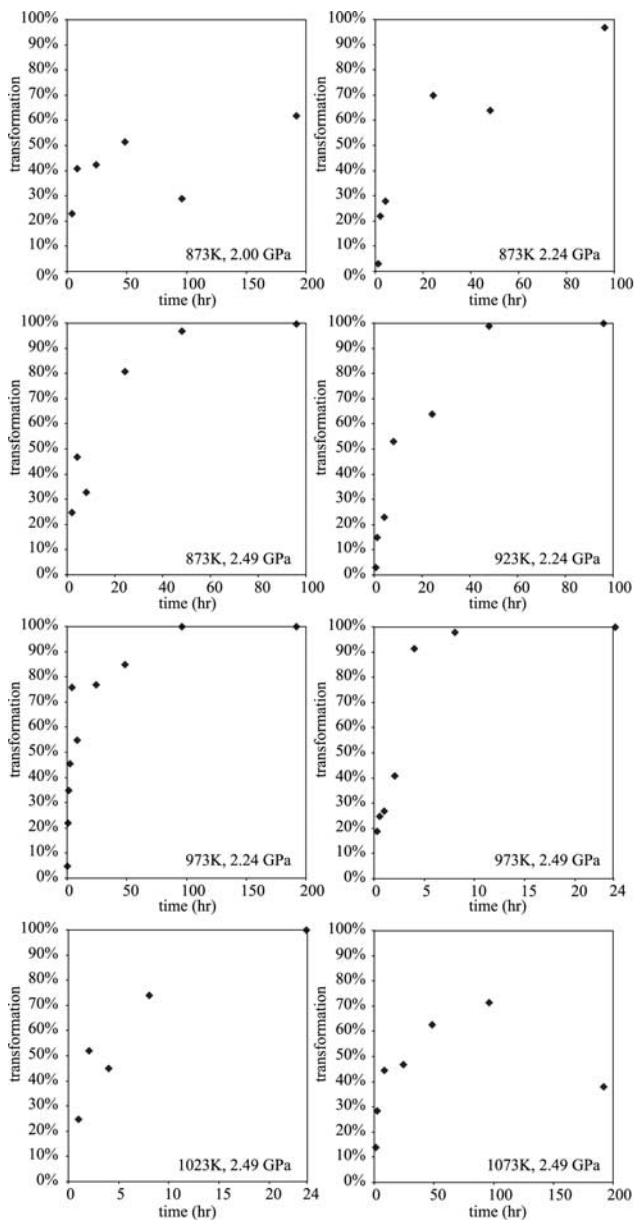


Figure 9. Rates of calcite → aragonite transformation measured as volume fraction of relict calcite fingers, diameter of calcite fingers, and spacing between calcite inclusions.

change of the reaction, and the rates of grain boundary or volume interdiffusion of Mg and Ca [Elliott, 1983; Lee *et al.*, 1988].

[38] In order for the texture we observed in Carrara marble to have formed, the transformation interface (i.e., the leading edge of a growing aragonite grain) must have moved through the rock faster than the Mg atoms that were being excluded from the growing aragonite could diffuse. If the Mg atoms could have moved faster than the interface propagated, by diffusing along the transformation interface or by diffusing through the calcite or aragonite grains, they could have escaped to form coarse grains of dolomite or Mg calcite and no cellular precipitation texture would have resulted.

[39] For all species for which calcite diffusion data are available, grain boundary diffusion is much faster than volume diffusion [Farver, 1994; Farver and Yund, 1996, 1998; Fisler and Cygan, 1999; Kronenberg *et al.*, 1984]. For example, volume diffusion of Ca and O are 6–8 orders of magnitude slower than grain boundary diffusion (assuming nominal grain boundary widths). These data imply that grain boundary diffusion dictated the initial spacing of the calcite inclusions in the aragonite. Grain boundary diffusion of Mg in calcite has not been measured, however, volume diffusion of Mg through calcite occurs at a rate that is intermediate between that of O and Ca, such that we can use the rates of O and Ca grain boundary diffusion as bounds for the rates of Mg grain boundary diffusion.

[40] The Mg self-diffusion measurements of Fisler and Cygan [1999] show that the characteristic diffusion distance

$$x_{\text{characteristic}} \approx \sqrt{Dt}$$

ranged from ~ 9 nm in the coldest and shortest of our experiments to ~ 2 μm in the hottest and longest experiments. This suggests that the volume diffusion of Mg should have been too slow to permit changes in inclusion size and spacing in all but the hottest (800°C) and longest (192 hours) experiments, but the trends in Figure 8 show instead that inclusion size and spacing did increase at all experimental conditions, mandating at least micron-scale Mg diffusion through the aragonite and faster diffusion than measured by Fisler and Cygan [1999].

[41] Metallurgists and ceramists, beginning with Cahm [1959], developed a formalism for understanding the growth of eutectoid and cellular precipitation textures based on the maximum rate of energy dissipation. Ashworth and Chambers [2000] used this theory to analyze magnetite + clinopyroxene intergrowths developed from the decomposition of olivine. They showed the following relationship among grain boundary diffusivity, D , grain boundary width, δ , interface velocity, v , volume of an included rod-shaped phase, p , and the inclusion spacing, λ :

$$\frac{8D\delta}{vp\lambda^2} > 1$$

For our experimental temperatures of 600 – 800°C , Farver and Yund [1998] reported $D\delta \approx 10^{-21}$ to 10^{-20} $\text{m}^3 \text{s}^{-1}$ for Ca grain boundary diffusion and $D\delta \approx 2 \times 10^{-25}$ to 3×10^{-23} $\text{m}^3 \text{s}^{-1}$ for O grain boundary diffusion in calcite. For calcite rod volume fractions $p = 0.10$ – 0.20 and calcite rod spacings $\lambda = 1$ – 4 (Table 2), the above relationship gives interface velocities of $v < 10^{-8}$ (O) to 10^{-12} (Ca) m s^{-1} at 600°C and $v < 10^{-7}$ (O) to 10^{-10} (Ca) m s^{-1} at 800°C . The growth rates that we measured in our Carrara marble samples lie between these two bounds, suggesting that the formalism of Ashworth and Chambers [2000] applies to our experiments. Specifically, the logarithms of our measured growth rates of aragonite are close to the logarithmic mean of the growth rates calculated from O and Ca grain boundary diffusivity in calcite:

$$\log v_{\text{measured}} = \frac{(\log v_{Ca} + \log v_O)}{2}$$

suggesting that to a good approximation, the logarithmic average of O and Ca grain boundary diffusivity can be applied to understanding intergrowth textures in natural marbles.

[42] The logarithmic growth rate measured in the “equant” textured samples is expected for a diffusion-controlled transformation in which the grain size of the product phase increases. The linear growth rates measured in the “rod” textured samples is expected for a diffusion-controlled transformation in which the grain size of the product phases (i.e., the eutectoid spacing) remains constant. Similar observations have been reported by *Kubo et al.* [2002]. The development of the “equant” texture only in samples with the smallest Gibbs free energy change suggests that the “rod” texture requires additional Gibbs free energy to overcome free energy costs associated with building the eutectoid texture [*Kubo et al.*, 2000].

4.2. Comparison With Naturally Transformed Marbles

[43] Eutectoid decomposition textures, similar to those produced in our experiments, have been reported from low-pressure/high-temperature marbles metamorphosed at ~480°C in the Hida Belt of Japan [*Imai et al.*, 1980] and from ultrahigh-pressure marbles metamorphosed at ~680°C in the Sulu Belt of China [*Ogasawara et al.*, 1998]. At both localities, during cooling, high-Mg calcite (3–4 wt % MgO) decomposed into dolomite + low-Mg calcite. The dolomite comprises rods, within the low-Mg calcite, that make up ~15 vol % of the transformed grains and are elongate perpendicular to the reaction front. This decomposition reaction occurred in calcite an order of magnitude richer in MgO than our Carrara marble, and thus the reaction products are those on the Mg side of the CaCO₃-MgCO₃ eutectoid, calcite + dolomite, rather than the phases on the Ca side found in our study. Written in parallel, these reactions have other important differences:

Carrara marble

low-Mg calcite → aragonite(enveloping phase)
+ Mg-calcite(rods)

Hida and Sulu

high-Mg calcite → low-Mg calcite(enveloping phase)
+ dolomite(rods)

In Carrara marble, the majority product phase has a different crystallographic structure and composition than the parent phase, and the rods are compositionally modified relicts of the parent. In the Asian marbles, the reverse is true. Applying the above equation from *Ashworth and Chambers* [2000]

$$\nu < \frac{8D\delta}{p\lambda^2}$$

to the Hida Belt marble, which has $p \approx 0.05$ and $\lambda \approx 150 \mu\text{m}$, and using the logarithmic mean of $D_{Ca}\delta$ and $D_{O}\delta$ reported by *Farver and Yund* [1998], the ~5 mm grains found at Hida could have grown in 6 Ma at 400°C or 0.1 Ma

at 500°C. The experiments reported in this study suggest that this same reasoning can be applied to other rocks for which the relevant diffusivities have been measured.

5. Conclusions

[44] We conducted phase equilibrium and kinetic experiments to document comprehensively the mechanisms and rates of the calcite → aragonite reaction in marble. Our reversal experiments, along with gas apparatus experiments of *Johannes and Puhan* [1971], define a new determination of the calcite ↔ aragonite equilibrium of P (GPa) = $2.4 \times 10^{-6} * (T - 298)^2$ (K) - $7.4 \times 10^{-4} * (T - 298)$ (K) + 0.299, with a pressure uncertainty of the boundary of about ±0.1 GPa. The transformation experiments showed surprisingly complex behavior. Trace amounts of MgO (0.36 wt %) fundamentally altered the reaction mechanism and texture. Nucleation occurred predominantly on grain boundaries, with each aragonite grain preferentially consuming the calcite grain with which it shared a c axis. At 600–750°C, the reaction zones consist of subequant aragonite grains containing relict intergrowths with the host calcite. The calcite relicts were stabilized by the presence of MgO in the starting material, which partitioned preferentially into the calcite. Over time, these calcite relicts underwent Ostwald ripening, diminishing in abundance, coarsening, and becoming more widely spaced. At 800°C, the aragonite neoblasts have a different, equant texture and contain relicts of calcite somewhat less enriched in MgO. The growth rates are in general agreement with theoretical predictions for cellular precipitation reactions, suggesting that extrapolation to natural processes is feasible if the relevant diffusivities have been measured.

[45] **Acknowledgments.** This project was supported by the U.S. Geological Survey and the National Science Foundation. Thanks to Ben Hankins, John Pinkston, and Laura Stern for laboratory support. Tom Sharp (Arizona State University) was instrumental in beginning the analytical electron microscopy while the first author was visiting the Universität Bayreuth. Helpful reviews were provided by Andreas Kronenberg, Tomoaki Kuba, and Tom Sisson.

References

- Ashworth, J. R., and A. D. Chambers (2000), Symplectic reaction in olivine and the controls of intergrowth spacing in symplectites, *J. Petrol.*, *41*, 285–304.
- Boettcher, A. L., and P. J. Wyllie (1968), The calcite-aragonite transition measured in the system CaO-CO₂-H₂O, *J. Geol.*, *76*, 314–330.
- Bohlen, S. R. (1984), Equilibria for precise pressure calibration and frictionless furnace assembly for the piston-cylinder apparatus, *Neues Jahrb. Mineral. Mitt.*, 404–412.
- Cahn, J. W. (1959), The kinetics of cellular segregation reactions, *Acta Metall.*, *7*, 18–28.
- Carlson, W. D. (1983), The polymorphs of CaCO₃ and the aragonite-calcite transformation, in *Carbonates: Mineralogy and Chemistry*, *Rev. Mineral.*, vol. 11, edited by R. J. Reeder, pp. 191–225, Mineral. Soc. of Am., Washington, D. C.
- Carlson, W. D., and J. L. Rosenfeld (1981), Optical determination of topotactic aragonite-calcite growth kinetics: Metamorphic implications, *J. Geol.*, *89*, 615–638.
- Dove, M. T., and B. M. Powell (1989), Neutron diffraction study of the tricritical orientational order/disorder phase transition in calcite at 1260K, *Phys. Chem. Miner.*, *16*, 503–507.
- Elliott, R. (1983), *Eutectic Solidification Processing*, 370 pp., Butterworths, London.
- Farver, J. R. (1994), Oxygen self-diffusion in calcite: Dependence on temperature and water fugacity, *Earth Planet. Sci. Lett.*, *121*, 575–587.
- Farver, J. R., and R. A. Yund (1996), Volume and grain boundary diffusion of calcium in natural and hot-pressed calcite aggregates, *Contrib. Mineral. Petrol.*, *123*, 77–91.

- Farver, J. R., and R. A. Yund (1998), Oxygen grain boundary diffusion in natural and hot-pressed calcite aggregates, *Earth Planet. Sci. Lett.*, *161*, 189–200.
- Fisler, D. K., and R. T. Cygan (1999), Diffusion of Ca and Mg in calcite, *Am. Mineral.*, *84*, 1392–1399.
- Friedman, G. M. (1959), Identification of carbonate minerals by staining methods, *J. Sediment. Petrol.*, *29*, 87–91.
- Gifkins, R. C. (1970), *Optical Microscopy of Metals*, 208 pp., Elsevier, New York.
- Gilman, J. J. (1960), Direct measurements of the surface energies of crystals, *J. Appl. Phys.*, *31*, 2208–2218.
- Hacker, B. R., and S. H. Kirby (1993), High-pressure deformation of calcite marble and its transformation to aragonite under non-hydrostatic conditions, *J. Struct. Geol.*, *15*, 1207–1222.
- Heard, H. C. (1972), Steady-state flow in polycrystalline halite at pressure of 2 kilobars, in *Flow and Fracture of Rocks*, *Geophys. Monogr. Ser.*, vol. 16, H. C. Heard et al., pp. 191–209, AGU, Washington, D. C.
- Holland, T. J. B., and R. Powell (1998), An internally consistent thermodynamic data set for phases of petrological interest, *J. Metamorph. Geol.*, *16*, 309–343.
- Imai, N., Y. Ogasawara, H. K. Lee, and J. Sakurai (1980), Micromorphological features of exsolved dolomite from the host magnesian calcite in some metamorphic carbonate rocks, as revealed by scanning electron microscopy, *Mem. Sch. Sci. Eng.*, *44*, pp. 71–89, Waseda Univ., Tokyo.
- Irving, A. J., and P. J. Wyllie (1975), Subsolidus and melting relationships for calcite, magnesite and the join $\text{CaCO}_3\text{--MgCO}_3$ to 36 kb, *Geochim. Cosmochim. Acta*, *39*, 35–53.
- Johannes, W., and D. Puhon (1971), The calcite-aragonite transition, reinvestigated, *Contrib. Mineral. Petrol.*, *31*, 28–38.
- Johannes, W., P. M. Bell, A. L. Boettcher, D. W. Chipman, J. F. Hays, H. K. Mao, R. C. Newton, and F. Seifert (1971), An inter-laboratory comparison of piston-cylinder pressure calibration using the albite-breakdown reaction, *Contrib. Mineral. Petrol.*, *32*, 24–38.
- Jull, M., and P. B. Kelemen (2001), On the conditions for lower crustal convective instability, *J. Geophys. Res.*, *106*, 6423–6445.
- Königsberger, E., J. Bugajski, and H. Gamsjäger (1989), Solid-solute phase equilibria in aqueous solution; II, A potentiometric study of the aragonite-calcite transition, *Geochim. Cosmochim. Acta*, *53*, 2807–2810.
- Kronenberg, A. K., R. A. Yund, and B. J. Giletti (1984), Carbon and oxygen diffusion in calcite: Effects of Mn content and PH_2O , *Phys. Chem. Miner.*, *11*, 101–112.
- Kubo, T., E. Ohtani, T. Kato, S. Urakawa, A. Suzuki, Y. Kanbe, K.-I. Funakoshi, W. Utsumi, and K. Fujino (2000), Formation of metastable assemblages and mechanisms of the grain-size reduction in the postspinel transformation of Mg_2SiO_4 , *Geophys. Res. Lett.*, *27*, 807–810.
- Kubo, T., E. Ohtani, T. Kondo, T. Kato, M. Toma, T. Hosoya, A. Sano, T. Kikegawa, and T. Nagase (2002), Metastable garnet in oceanic crust at the top of the lower mantle, *Nature*, *420*, 803–807.
- Lee, H. J., G. Spanos, G. J. Shiflet, and H. I. Aaronson (1988), Mechanisms of the bainite (non-lamellar eutectoid) reaction and a fundamental distinction between the bainite and pearlite (lamellar eutectoid) reactions, *Acta Metall.*, *36*, 1129–1140.
- Ludwig, K. R. (2001), Isoplot/EX, rev. 2.49. A geochronological toolkit for Microsoft Excel, *Spec. Publ. 1a*, Berkeley Geochronol. Cent., Berkeley, Calif.
- Murr, L. E. (1975), *Interfacial Phenomena in Metals and Alloys*, 376 pp., Addison-Wesley, Boston, Mass.
- Ogasawara, Y., R. Y. Zhang, and J. G. Liou (1998), Petrogenesis of dolomitic marbles from Rongcheng in the Su-Lu ultrahigh-pressure metamorphic terrane, eastern China, *Island Arc*, *7*, 82–97.
- Ostwald, W. (1897), Studien über die Bildung und Umwandlung fester Körper, *Z. Phys. Chem.*, *22*, 289–302.
- Powell, R., and T. J. B. Holland (1988), An internally consistent dataset with uncertainties and correlations: 3. Applications to geobarometry, worked examples and a computer program, *J. Metamorph. Geol.*, *6*, 173–204.
- Powell, R., T. Holland, and B. Worley (1998), Calculating phase diagrams involving solid solutions via non-linear equations, with examples using THERMOCALC, *J. Metamorph. Geol.*, *16*, 577–588.
- Redfern, S. A. T., E. Salje, and A. Navrotsky (1989), High-temperature enthalpy at the orientational order-disorder transition in calcite: Implications for the calcite/aragonite phase equilibrium, *Contrib. Mineral. Petrol.*, *101*, 479–484.
- Rubie, D. C., and P. E. Champness (1987), The evolution of microstructure during the transformation of Mg_2GeO_4 olivine to spinel, *Bull. Mineral.*, *110*, 471–480.
- Rubie, D. C., and C. R. Ross (1994), Kinetics of the olivine-spinel transformation in subducting lithosphere: Experimental constraints and implications for deep slab processes, *Earth Planet. Sci. Lett.*, *86*, 223–241.
- Rubie, D. C., and A. B. Thompson (1985), Kinetics of metamorphic reactions at elevated temperatures and pressures: An appraisal of available experimental data, in *Advances in Physical Geochemistry*, edited by A. B. Thompson and D. C. Rubie, pp. 27–79, Springer, New York.
- Spencer, C. W., and D. J. Mack (1962), Eutectoid transformations in nonferrous and ferrous alloy systems, in *Decomposition of Austenite by Diffusional Processes*, edited by V. F. Zackay and H. I. Aaronson, pp. 549–606, John Wiley, New York.
- Sundquist, B. E. (1973), Cellular precipitation, *Metall. Trans.*, *4*, 1919–1934.
- Turnbull, D. (1956), Phase changes, *Solid State Phys.*, *3*, 225–306.
- Veizer, J. (1978), Secular variations in the composition of sedimentary carbonate rocks, II. Fe, Mn, Ca, Mg, Si and minor constituents, *Precambrian Res.*, *6*, 381–413.
- Wenk, H.-R. (1985), Carbonates, in *Preferred Orientation in Deformed Metals and Rocks: An Introduction to Modern Texture Analysis*, edited by H.-R. Wenk, pp. 361–383, Springer, New York.
- S. R. Bohlen, Joint Oceanographic Institutions, Washington, DC 20192, USA.
- B. R. Hacker, Department of Geological Sciences, University of California, Santa Barbara, CA 93106-9630, USA. (hacker@geol.ucsb.edu)
- S. H. Kirby, U.S. Geological Survey, Menlo Park, CA 94025, USA.
- D. C. Rubie, Bayerisches Geoinstitut, Universität Bayreuth, D-95490, Bayreuth, Germany.